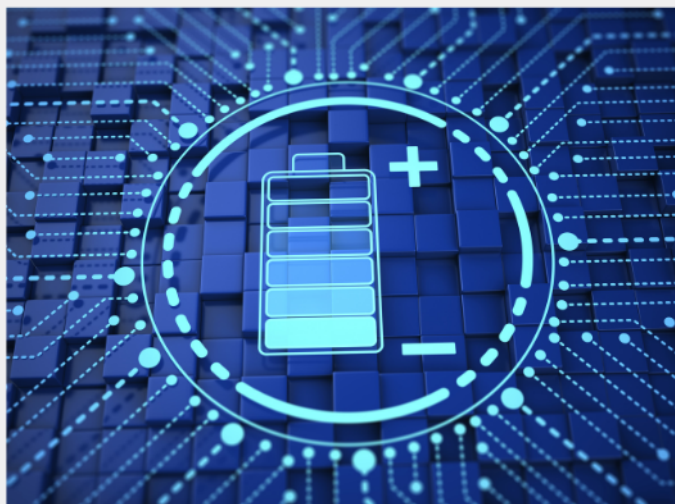




# Exploring the possibilities of increasing energy density and efficiency in rechargeable batteries

Download this complimentary article collection



The exponential rise in the need for better, more efficient power sources has sparked an incredible amount of research into batteries. A primary focus of research has been increasing the energy density of batteries, as it allows for lighter, more portable storage of energy. Lithium-ion batteries, for example, have a much higher energy density than conventional lead-acid batteries and can be used for various purposes, such as in electric vehicles.

This article collection provides a comprehensive list of references for new methods and technologies for increasing the energy density of batteries.

# Modulation of Alkyl Chain Length on the Thiazole Side Group Enables Over 17% Efficiency in All-Small-Molecule Organic Solar Cells

Kangqiao Ma, Wanying Feng, Huazhe Liang, Hongbin Chen, Yuxin Wang, Xiangjian Wan, Zhaoyang Yao, Chenxi Li, Bin Kan,\* and Yongsheng Chen\*

Molecular innovation is highly desirable to achieve efficient all-small-molecule organic solar cells (SM-OSCs). Herein, three small-molecule donors (SMDs) with alkylated thiazole side groups (namely BO-1, HD-1, and OD-1), which differ only in the alkyl side chain are reported. Although these SMDs possess similar absorption profiles and molecular energy levels, their crystallinity and miscibility with BTP-eC9 slightly decrease along with the elongation of the alkyl side chain. After blending with BTP-eC9, different miscibility leads to different degrees of phase separation. Among these SM-OSCs, the HD-1-based device shows a decent bulk-heterojunction (BHJ) morphology with proper phase separation and more dynamic carrier behavior. Thus, compared to the BO-1 and OD-1-based devices, the HD-1-based device achieves a higher short-circuit current of 26.04 mA cm<sup>-2</sup> and a fill factor of 78.46%, leading to an outstanding PCE of 17.19%, which is one of the highest values among SM-OSCs. This work provides a rational design strategy of SMDs for highly efficient SM-OSCs.

role in improving power conversion efficiencies (PCEs). From the perspective of chemical structures, the active layer materials are divided into polymers and small molecules. Compared to conjugated polymer materials, conjugated small-molecule materials have obvious advantages, such as well-defined chemical structure, negligible batch-to-batch variation, low energetic disorder, and so on.<sup>[7–9]</sup> Though the state-of-the-art polymer-based OSCs (PSCs) have realized impressive PCEs of over 19%, it is necessary to prompt the development of all-small-molecule organic solar cells (SM-OSCs) to fully exploit their aforementioned advantages.<sup>[10–12]</sup>

In the early stage of SM-OSCs, our group developed a series of acceptor-donor-acceptor (A-D-A) type small-molecule donors (SMDs), and achieved impressive PCEs over 10% in the fullerene<sup>[13–14]</sup> and over 15% in the non-fullerene based SM-OSCs.<sup>[15]</sup> Recently, with the emergence of the low bandgap small-molecule acceptor Y6 and its derivatives, great progresses with PCEs over 17% has been witnessed in the SM-OSCs using the A-D-A structured SMDs, but the performance of SM-OSCs still lags behind PSCs.<sup>[16–19]</sup> As Proved by the development of OSCs in the past decades, material innovation is always the key to improving photovoltaic performance.<sup>[4,5,20]</sup> Thus, understanding the relationship between molecular structure and device performance to develop novel SMDs is highly desirable to enhance the PCEs of SM-OSCs.<sup>[21,22]</sup> On the other hand, obtaining an ideal BHJ morphology is still a great challenge in fabricating SM-OSCs, which is one of the major reasons for the relatively inferior performance of SM-OSCs.<sup>[23,24]</sup> From the aspect of morphology control, the morphology of small molecules is more tricky to tune compared with polymers due to their stronger crystallinity. For some high-performance polymer donors (PM6, D18, etc.), their unique pre-aggregation feature in the solution plays a pivotal role in the formation of the desirable interpenetrating network in the corresponding photoactive blend film;<sup>[25,26]</sup> however, since the lack of strong intermolecular entanglement and intermolecular interaction, it is more challenging for SMDs to form the comparable morphology in blend film.<sup>[27]</sup> Tuning the morphology of the active layer by optimizing the alkyl chain of SMDs has been proven to be

## 1. Introduction

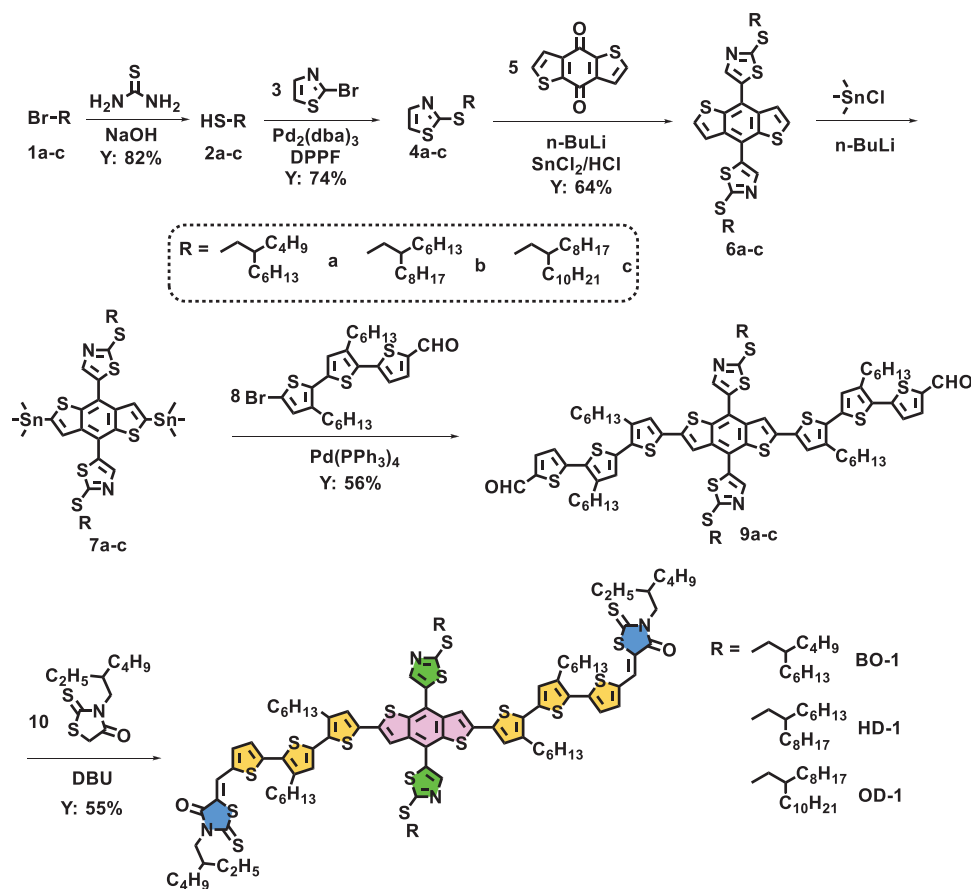
Bulk-heterojunction (BHJ) organic solar cells (OSCs) have attracted great attention due to their outstanding advantages of being lightweight, flexible, and capable of being prepared in large areas via solution processing methods.<sup>[1–6]</sup> In BHJ-OSCs, the active layer is composed of electron donor and electron acceptor materials, which play the most important

K. Ma, W. Feng, H. Liang, H. Chen, Y. Wang, X. Wan, Z. Yao, C. Li, Y. Chen  
State Key Laboratory and Institute of Elemento-Organic Chemistry  
The Centre of Nanoscale Science and Technology and Key Laboratory of  
Functional Polymer Materials  
Renewable Energy Conversion and Storage Center (RECAST)  
College of Chemistry  
Nankai University  
Tianjin 300071, China  
E-mail: yschen99@nankai.edu.cn

B. Kan  
School of Materials Science and Engineering  
National Institute for Advanced Materials  
Nankai University  
Tianjin 300350, China  
E-mail: kanbin04@nankai.edu.cn

 The ORCID identification number(s) for the author(s) of this article can be found under <https://doi.org/10.1002/adfm.202214926>.

DOI: 10.1002/adfm.202214926



**Scheme 1.** The synthetic route of three small molecule donors (BO-1, HD-1, and OD-1).

an effective method.<sup>[28–30]</sup> A proper alkyl chain not only determines the molecule's solubility but also modulates the domain size and phase separation of the active layer.<sup>[30,31]</sup> Recently, our group developed a highly efficient SMD, SW2, which employed thiazole substituents as the side groups of the benzodithiophene (BDT) central unit.<sup>[15]</sup> After blending with acceptor Y6, SW2 exhibited compact and ordered molecular packing and achieved a well-tuned BHJ morphology, resulting in low recombination and high charge mobility. Consequently, the SW2:Y6-based device afforded a PCE of 15.51%, which was among the best SM-OSCs.

In this contribution, to further exploit the potential of this kind of SMDs in SM-OSCs, side chain engineering on the thiazole unit was performed to further optimize the physicochemical and photovoltaic properties of this type of SMDs. Herein, three SMDs (BO-1, HD-1, and OD-1) were reported, with different alkyl chains in the thiazole side group. The length of alkyl chains has a marginal impact on their light absorption and energy levels, but significantly impacts their crystallinity which is gradually decreased along with the increase of the length of side group alkyl chains. When blending with small-molecule acceptor BTP-eC9, the corresponding optimal devices showed PCEs of 16.79%, 17.19%, and 15.18% for BO-1, HD-1, and OD-1-based devices, respectively. The impressive PCE of 17.19% based on HD-1:BTP-eC9 is one of the highest values for binary SM-OSCs to date. This work reveals that the thiazole

side groups have great potential in designing highly efficient SM-OSCs, and the molecular crystallinity can be precisely controlled by adjusting the alkyl chain to optimize the film morphology.

## 2. Results and Discussion

### 2.1. Synthesis and Characterizations

The synthetic route of three SMDs is presented in **Scheme 1**. Compounds 1a–c, 3, 5, 8, and 10 are purchased and used without any purification. Compounds 2a–c were synthesized according to the literature.<sup>[32]</sup> Afterward, the BDT derivations with different alkylthiol-substituted thiazole side-chains (compounds 6a–c) were synthesized by the two-step reactions with satisfactory yields. Subsequently, compounds 6a–c were treated by n-butyllithium to obtain the stannanes 7a–c, which were used to prepare the dialdehyde compound 9a–c via the Stille coupling reaction. Finally, BO-1, HD-1, and OD-1 were obtained via a Knoevenagel condensation with compounds 9a–c and 3-(2-ethylhexyl)-2-thioxothiazolidin-4-one, respectively. The detailed synthetic procedures and the nuclear magnetic resonance (NMR) spectra were presented in the Supporting Information. The thermogravimetric analysis (TGA) measurements demonstrate that these molecules have good

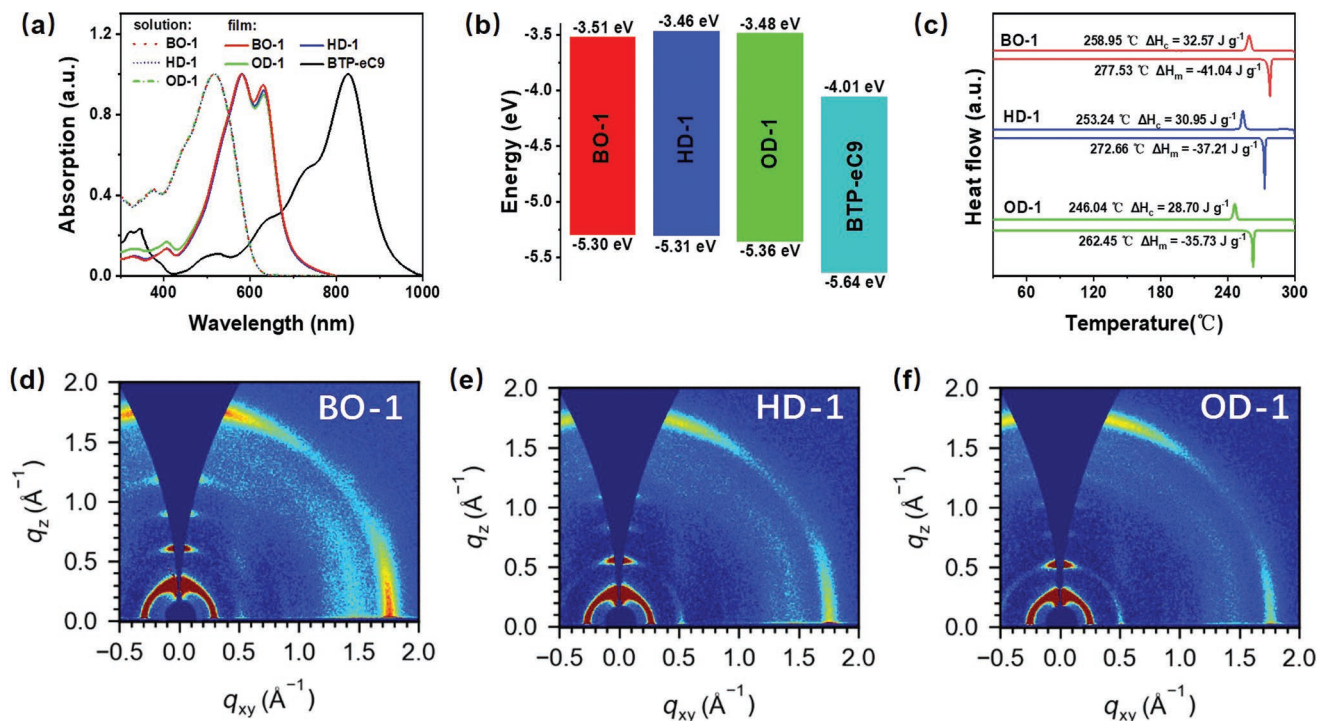


**Figure 1.** a) The absorption spectra of BO-1, HD-1, and OD-1 in chloroform solutions and solid films; b) The energy alignments of three SMDs and BTP-eC9; c) The DSC curves of BO-1, HD-1, and OD-1 at a heating and cooling rate of 10 °C min<sup>-1</sup> under nitrogen flow; d–f) The 2D GIWAXS patterns of BO-1, HD-1, and OD-1 pristine films, respectively.

thermal stability with 5% weight loss at 354, 362, and 348 °C for BO-1, HD-1, and OD-1, respectively (Figure S1, Supporting Information).

## 2.2. Optical, Electrochemical, and Crystalline Properties

As illustrated in **Figure 1a**, these three SMDs exhibit almost identical absorption profiles with a maximum absorption wavelength ( $\lambda_{\text{max}}$ ) at 518 nm in their dilute chloroform solutions, which suggests that the alkyl chain has little influence on the behavior of molecules in dilute solution. Meanwhile, from solutions to films, all of them display same red-shift with their  $\lambda_{\text{max}}$  at 580 nm accompanied by obvious shoulder peaks located at  $\approx 630$  nm, implying their stronger intermolecular interaction and  $\pi$ - $\pi$  stacking behaviors in the films. It should be noted that the ratios of 0-0/0-1 vibronic peak show a gradually decreased trend from 0.95 of BO-1 to 0.92 of HD-1 to 0.90 of OD-1 (Figure S2, Supporting Information), which is ascribed to the fact that the length of alkyl chain affects their intermolecular interaction, crystallinity, and aggregation behaviors.<sup>[18]</sup> The differential scanning calorimetry (DSC) measurements were used to investigate the crystalline property of those SMDs. As shown in **Figure 1c**, the melting points (m.p.) and enthalpies of BO-1, HD-1, and OD-1 are shifted from 277.53 °C ( $-41.04$  J g<sup>-1</sup>) to 272.66 °C ( $-37.21$  J g<sup>-1</sup>) and 262.45 °C ( $-35.73$  J g<sup>-1</sup>), suggesting the intermolecular interaction and crystallinity of the three compounds gradually decrease with the bulking of the alkyl chains on the side groups.

Cyclic voltammetry was conducted to evaluate the highest occupied molecular orbital (HOMO) and lowest unoccupied molecular orbital (LUMO) energy levels of these molecules in solid state, and their oxidation and reduction curves are shown in **Figure S3** (Supporting Information). According to the equation of  $E_{\text{HOMO/LUMO}} = -(E_{\text{ox/red}} - E_{\text{Fc/Fc}^{+1}} / 2 + 4.8)$  eV,<sup>[33]</sup> the HOMO/LUMO energy levels of BO-1, HD-1, and OD-1 were calculated to be  $-5.30/-3.51$ ,  $-5.31/-3.46$  and  $-5.36/-3.48$  eV, respectively. As illustrated in **Figure 1b**, the HOMO energy levels of BO-1, HD-1, and OD-1 slightly decrease with the elongation of the side chains. However, the LUMO energy levels of the three donors have a very small increase, reflected in the slightly increased electrochemical  $E_g$  from 1.79, 1.85 to 1.88 eV for BO-1, HD-1, and OD-1, respectively. However, as shown in **Figure 1a** and **Table 1**, their optical  $E_g$  stays almost the same  $\approx 1.72$ – $1.73$  eV. The small difference between the electrochemical  $E_g$  and the optical  $E_g$  should reflect the measure of the electron-hole pair binding energy.<sup>[33]</sup> Importantly, the  $\Delta E_{\text{HOMO}}$  and  $\Delta E_{\text{LUMO}}$  between SMDs and the acceptor BTP-eC9 are large enough to achieve efficient exciton dissociation.<sup>[34,35]</sup>

Grazing incidence wide-angle X-ray scattering (GIWAXS) measurements were performed to investigate the molecular stacking and orientations of SMDs in the neat films. As shown in **Figure 1d–f**, all three SMDs exhibit obvious  $\pi$ - $\pi$  stacking (010) and lamella stacking (100) diffraction peaks in the in-plane (IP) and the out-of-plane (OOP) directions, which is indicative of edge-on and face-on coexisting orientations in their pristine films.<sup>[36,37]</sup> Meanwhile, multiple higher-order (h00) diffraction peaks in the OOP direction are observed in their neat films, suggesting the long-range order and decent crystallinity

**Table 1.** The optical and electrochemical properties of small-molecule donors.

SMDs	$\lambda_{\text{max}}^{\text{sol}}$ [nm]	$\lambda_{\text{max}}^{\text{film}}$ [nm]	$\lambda_{\text{onset}}$ [nm]	$E_{\text{g}}^{\text{opt(a)}}$ [eV]	$E_{\text{g}}^{\text{CV(b)}}$ [eV]	HOMO [eV]	LUMO [eV]
BO-1	517	580, 630	719	1.72	1.79	-5.30	-3.51
HD-1	518	582, 631	718	1.73	1.85	-5.31	-3.46
OD-1	516	581, 632	718	1.73	1.88	-5.36	-3.48

<sup>a)</sup> $E_{\text{g}}^{\text{opt}}$  is estimated by the equation  $E_{\text{g}} = 1240/\lambda_{\text{onset}}$ ; <sup>b)</sup> $E_{\text{g}}^{\text{CV}}$  is estimated by the difference between HOMO and LUMO energy levels.

properties of these SMDs.<sup>[38]</sup> It is worth mentioning that the integral intensity of (100) peak in the IP direction is increasing but in the OOP direction is decreasing from BO-1, HD-1, to OD-1 (Figure S4, Supporting Information). Generally, the relative crystallinity of film is assessed by diffraction peak area, and the increased peak area indicates higher crystallinity.<sup>[39]</sup> These results indicate that the content of face-on orientation increases with the elongation of the alkyl chain. Although BO-1, HD-1, and OD-1 have almost the same  $\pi$ - $\pi$  stacking distance of 3.53 Å, calculated from their (010) peaks at 1.78 Å<sup>-1</sup> in the OOP direction, their coherence length (CCL) of  $\pi$ - $\pi$  stacking in the OOP direction increased from 46.19 Å to 48.18 Å to 50.81 Å (Tables S1 and S2, Supporting Information). Their lamellar stacking distances, estimated from their (100) peaks in the OOP direction, become longer along with the increase of their side chains from 2-butyloctyl of BO-1 to 2-octyldecanyl of OD-1. Similar trends are observed from their (010) diffraction peak and (100) peak in the IP direction. The above results suggest the shorter the alkyl chain is, the tighter the molecules pack, which supports the observed results from DSC measurements.

### 2.3. Device Performance

To study the photovoltaic performance of three donors, non-fullerene acceptor BTP-eC9 was adopted and SM-OSCs were fabricated with a conventional device structure of ITO/PEDOT:PSS/SMDs:BTP-eC9/PDINO/Ag (Figure 2a). The ratios of donor-to-acceptor and thermal annealing temperature of the photoactive layers were carefully optimized, and 2-iodinenaphthalene (2-IN) was used as the solvent additive (Tables S3–S5, Supporting Information). The current density-voltage ( $J$ - $V$ ) and external quantum efficiency (EQE) curves of the optimal SM-OSCs are presented in Figure 2b,c, and

the corresponding photovoltaic parameters are collected in Table 2. All of the optimal devices achieve high PCEs over 15%. Although their HOMO energy levels gradually down-shifted from BO-1, HD-1 to OD-1, the corresponding open-circuit voltages ( $V_{\text{OC}}$ ) decreased, which could be attributed to their different energy losses ( $E_{\text{loss}}$ s) as discussed below. Overall, the device based on HD-1 shows a remarkable PCE of 17.19% with a  $V_{\text{OC}}$  of 0.842 V, a short-current density ( $J_{\text{SC}}$ ) of 26.04 mA cm<sup>-2</sup>, and an excellent FF of 78.46%. To our knowledge, the obtained PCE is one of the highest values for SM-OSCs to date.<sup>[16,18,19]</sup> The device based on BO-1 with the shorter side chains also exhibits a high PCE of 16.79% with a similar  $V_{\text{OC}}$  of 0.845 V and an FF of 77.74%, but with a slightly decreased  $J_{\text{SC}}$  of 25.56 mA cm<sup>-2</sup>. When prolonging the side chains into 2-octyldecanyl, the PCE of OD-1-based device drastically dropped to 15.18%, mainly originating from its lower FF of 71.89%. Compared with BO-1 and OD-1, the HD-1-based device has higher  $J_{\text{SC}}$  and FF, which should be mainly attributed to their different BHJ morphologies as explained below. The external quantum efficiency (EQE) curves were measured to verify their different  $J_{\text{SC}}$  values. As shown in Figure 2c, although all devices had the same photo response region from 300 to 950 nm, HD-1-based device exhibits significantly higher EQE responses in the whole region than those of BO-1 and OD-1-based devices, suggesting a more efficient photoelectric conversion process in the HD-1 optimal device. The integrated  $J_{\text{SC}}$  values from the EQE spectra are 25.16, 25.61, and 24.97 mA cm<sup>-2</sup> for BO-1, HD-1, and OD-1-based devices, consistent with the values obtained from their  $J$ - $V$  curves. Moreover, the device performances based on HD-1:BTP-eC9 with thick films have been listed in Table S6 and Figure S5 (Supporting Information). When the film thickness-based HD-1:BTP-eC9 reaches 350 nm, a high PCE  $\approx$ 15% can still be obtained, which is beneficial for future commercial preparation.

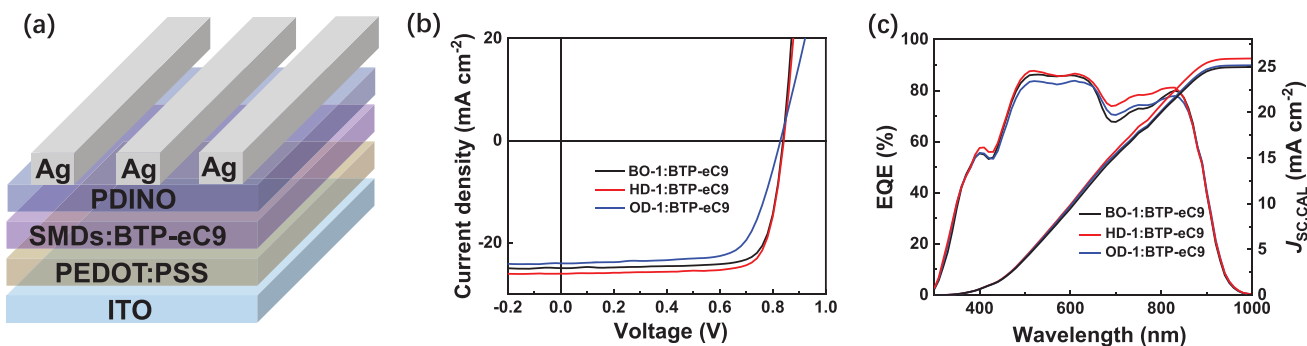


**Figure 2.** a) The device structure of SM-OSCs. b) The  $J$ - $V$  characteristics and c) EQE spectra of the SMDs-based devices.

**Table 2.** Optimized device performance data of BO-1, HD-1, and OD-1 as donor and BTP-eC9 as acceptor under the illumination of AM 1.5 G, 100 mW cm<sup>-1</sup>.

Active layers	$V_{OC}$ [V] <sup>a)</sup>	FF [%]	$J_{SC}$ [mA cm <sup>-2</sup> ]	$J_{SC}^{(calb)}$ [mA cm <sup>-2</sup> ]	PCE [%]
BO-1:BTP-eC9	0.845 (0.844 ± 0.001)	77.74 (77.22 ± 0.41)	25.56 (25.50 ± 0.17)	25.16	16.79 (16.61 ± 0.11)
HD-1:BTP-eC9	0.842 (0.840 ± 0.001)	78.46 (78.28 ± 0.24)	26.04 (25.98 ± 0.04)	25.61	17.19 (17.06 ± 0.09)
OD-1:BTP-eC9	0.828 (0.828 ± 0.002)	71.89 (71.85 ± 0.50)	25.49 (25.03 ± 0.30)	24.97	15.18 (14.89 ± 0.16)

<sup>a)</sup>The average photovoltaic parameters calculated from 15 independent devices; <sup>b)</sup>Current densities calculated from EQE curves.

## 2.4. Energy Losses Analysis

To understand the difference in  $V_{OC}$  values of three devices, their energy losses ( $E_{loss}$ ) were investigated, and the detailed parameters are collected in Table S7 (Supporting Information). The total  $E_{loss}$  of the photovoltaic cell can be determined by the energy offsets between the optical band gaps ( $E_g$ ) and  $qV_{OC}$ , following the equation of  $E_{loss} = E_g - qV_{OC}$ .<sup>[40]</sup> Here, the  $E_g$  of the OSCs was calculated from the intersections of the normalized UV-vis absorption and photoluminescence (PL) spectra of the low-bandgap acceptor BTP-eC9.<sup>[41,42]</sup> As presented in Figure S6 (Supporting Information), the  $E_g$  of the blend films based on BO-1, HD-1, and OD-1 were 1.388, 1.387, and 1.387 eV, respectively. According to the theory of detailed balance,<sup>[43]</sup> the  $E_{loss}$  can be divided into three parts ( $E_{loss} = \Delta E_1 + \Delta E_2 + \Delta E_3$ ). The first term,  $\Delta E_1 = E_g - qV_{OC}^{SQ}$ , is defined as the difference between the  $E_g$  and the maximum voltage based on the Shockley-Queisser (SQ) limit ( $qV_{OC}^{SQ}$ ).<sup>[41,44]</sup> This component  $E_{loss}$  caused by radiative recombination loss originates from absorption above the bandgap, which is inevitable in all types of solar cells. The  $qV_{OC}^{SQ}$  was calculated to be 1.126, 1.124, and 1.124 eV for BO-1, HD-1, and OD-1-based devices, respectively. Here, all devices exhibited similar  $\Delta E_1$  values of  $\approx 0.263$  eV. The second term,  $\Delta E_2 = qV_{OC}^{SQ} - qV_{OC}^{rad}$ , stems from absorption below the bandgap. The  $qV_{OC}^{rad}$  is the open circuit voltage when there is only radiative recombination, which can be estimated from the Fourier transform photocurrent spectroscopy external quantum efficiency (FTPS-EQE) spectra of OSCs using equation below. The radiative recombination limit for the saturation current ( $J_0^{rad}$ ) is also calculated from the EQE spectrum using the detailed balance theory,<sup>[43,45]</sup> and  $\Phi_{BB}$  represents the black body spectrum at 298 K.

$$V_{OC}^{rad} = \frac{KT}{q} \ln \left( \frac{J_{SC}}{J_0^{rad}} + 1 \right) \quad (1)$$

$$J_0^{rad} = q \int EQE(E) \Delta_{BB}(E) dE \quad (2)$$

As shown in Table S7 (Supporting Information), the  $qV_{OC}$  values of the SM-OSCs based on BO-1, HD-1, and OD-1 were calculated to be 1.061, 1.057, and 1.060 V, respectively, which corresponded to  $\Delta E_2$  values of 0.065, 0.067, and 0.064 V, respectively. The third term,  $\Delta E_3 = qV_{OC}^{rad} - qV_{OC}$ , originates from non-radiative recombination loss. In addition,  $\Delta E_3$  can be obtained from the EQE of EL (EQE<sub>EL</sub>) according to equation  $\Delta E_3 = -kT \ln(EQE_{EL})$ .<sup>[46]</sup> As summarized in Figure 3b, the  $\Delta E_3$  values calculated from two different methods show similar variation tendencies for the three SM-OSCs. It is apparent that the length of the alkyl chain has little impact on  $\Delta E_1$  and  $\Delta E_2$

values, however, the  $\Delta E_3$  value increases with the extension of the alkyl chain from BO-1, HD-1 to OD-1. It was found that the SM-OSCs based on BO-1 exhibited the smallest  $\Delta E_3$  value of 0.216 V, which is consistent with the results that the device based on BO-1 obtains the highest  $V_{OC}$ . Although OD-1 has the deepest HOMO level, its  $V_{OC}$  is lower than those of the other two devices, which can be attributed to its largest  $\Delta E_3$  value.

## 2.5. Charge Dynamic Analysis

The measurement of the photogenerated current density ( $J_{ph}$ ) against the effective voltage ( $V_{eff}$ ) was carried out to understand the exciton dissociation and charge collection in SM-OSCs (Figure 3c).<sup>[47]</sup> Based on the reported methods, the exciton dissociation probability ( $P_{diss}$ ) of the HD-1-based device was estimated to be 0.974, which is slightly higher than BO-1 and OD-1-based devices. Moreover, the charge collection probability ( $P_{coll}$ ) of HD-1-based devices was estimated to be 0.890, which is higher than the other two optimal devices (0.872 for BO-1 and 0.861 for OD-1-based devices, respectively). These results indicate that more efficient photogenerated exciton dissociation and charge collection occurred in HD-1-based devices, consistent with its higher  $J_{SC}$ . Besides, the  $P_{light}$  dependence of  $J_{SC}$ , which can be described as  $J_{SC} \propto P_{light}^S$ , is conducted to analyze the charge recombination mechanism (Figure 3d).<sup>[48]</sup> The power-law exponent  $S$  reflects the bimolecular charge recombination condition in the device. All the devices show  $S$  values close to 1, suggesting their similar and weak bimolecular recombination behaviors.

To further understand the charge recombination and extraction behaviors, transient photocurrent (TPC) and transient photovoltage (TPV) are applied to characterize these devices.<sup>[49]</sup> As shown in Figure S7 (Supporting Information), the device based on HD-1:BTP-eC9 shows a faster extraction time of 0.33  $\mu$ s, shorter than that of the BO-1-based device (0.37  $\mu$ s), and the OD-1-based device (0.42  $\mu$ s). Furthermore, the carrier lifetimes ( $\tau$ ) derived from the TPV measurements of the BO-1, HD-1, and OD-1-based devices are 69, 110, and 57  $\mu$ s (Figure 3e), respectively. The longest  $\tau$  of HD-1-based device indicates the minimum charge recombination occurred in the corresponding device. The charge carrier mobility of these blended films was estimated by the space-charge-limited current (SCLC) measurements.<sup>[50]</sup> As shown in Figure 3f, the BO-1:BTP-eC9 blend displayed a hole mobility ( $\mu_h$ ) of  $1.03 \times 10^{-3}$  cm<sup>2</sup> V<sup>-1</sup> s<sup>-1</sup> and an electron mobility ( $\mu_e$ ) of  $1.23 \times 10^{-3}$  cm<sup>2</sup> V<sup>-1</sup> s<sup>-1</sup>. As the side alkyl chains extended to 2-hexadecyl, the HD-1:BTP-eC9 blend exhibited simultaneously improved  $\mu_h$  and  $\mu_e$  of  $1.14 \times 10^{-3}$  and  $1.32 \times 10^{-3}$  cm<sup>2</sup> V<sup>-1</sup> s<sup>-1</sup>, respectively. Meanwhile, a decreased  $\mu_h$

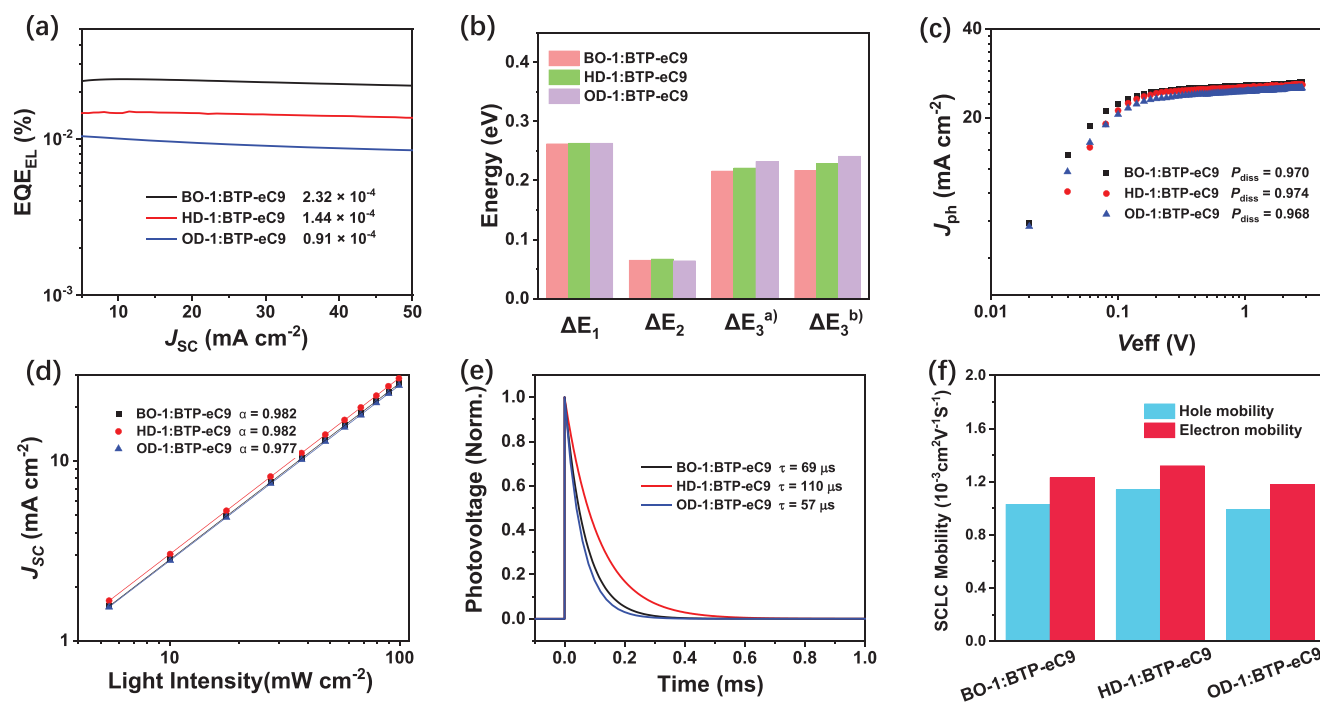


**Figure 3.** a) The EQE<sub>EL</sub> spectra for optimized SM-OSCs. b) The energy loss of three devices,  $\Delta E_3^a$ ) calculated from  $qV_{\text{rad OC}} - qV_{\text{OC}}$ ,  $\Delta E_3^b$ ) calculated from  $-kT \ln(\text{EQE}_{\text{EL}})$ . c)  $J_{\text{ph}}-V_{\text{eff}}$  curves, d)  $J_{\text{SC}}$  versus  $P_{\text{light}}$  relationships, and e) Transient photovoltage measurement for optimized SM-OSCs. f) Hole and electron mobilities for three blend films.

of  $0.99 \times 10^{-3} \text{ cm}^2 \text{ V}^{-1} \text{ s}^{-1}$  and  $\mu_e$  of  $1.18 \times 10^{-3} \text{ cm}^2 \text{ V}^{-1} \text{ s}^{-1}$  were observed for the OD-1:BTP-eC9 blend. Detailed parameters are summarized in Figure S8 and Table S8 (Supporting Information). The HD-1:BTP-eC9 film demonstrated not only higher but more balanced charge carrier mobility ( $\mu_h/\mu_e = 0.86$ ) than the other two blend films. All factors mentioned above benefit the improvement of the  $J_{\text{sc}}$  and FF of the HD-1-based device, leading to its enhanced performance.

## 2.6. BHJ Morphology Investigation

To further understand their different device performance, the surface morphologies of the blend films were investigated by atomic force microscopy (AFM). The root mean square (RMS) roughness values of the devices of HD-1:BTP-eC9 (0.57 nm) are slightly lower than the devices of BO-1:BTP-eC9 (0.72 nm) and OD-1:BTP-eC9 (0.81 nm) (Figure S9, Supporting Information). As shown in Figure 4a, the HD-1:BTP-eC9 blend exhibits much-refined morphology featured with a typical fibril network with appropriate phase separation, which is supposed to be the key to its efficient charge separation and extraction process. In contrast, BO-1:BTP-eC9 blend film exhibits weak phase separation, and OD-1:BTP-eC9 blend film shows a large-sized aggregation distribution. Generally, in three donor-acceptor blend films, the phase separation gradually becomes larger with the elongation of the side chain. This may be attributed to the fact that shorter alkyl chains decrease the space between molecular backbones, thus reducing the molecular motion and rotation space during the film formation, and consequently leading to weaker aggregation tendency.<sup>[19]</sup>

Furthermore, contact angle experiments were performed to investigate the miscibility of three donors and BTP-eC9. Figure S10 (Supporting Information) shows the images of water and glycerol droplets on their neat films, and the corresponding results including the surface tensions ( $\gamma$ ) and Flory-Huggins interaction parameters ( $\chi$ )<sup>[26,51]</sup> were summarized in Figure S11 and Table S9 (Supporting Information). The  $\gamma$  for BO-1, HD-1, OD-1, and BTP-eC9 are estimated to be 22.41, 22.14, 21.78, and 28.99 mN m<sup>-1</sup>, respectively; the calculated  $\chi$  for BO-1, HD-1, and OD-1-based blends are 0.42, 0.46, and 0.51, respectively. The lower  $\chi$  value represents better miscibility of two components. Thus, the miscibility of BO-1, HD-1, OD-1, and BTP-eC9 gradually decreases along with the elongation of the alkyl chain, which might lead to a large phase separation as observed in the AFM image. These results prove that side chain engineering of SMDs has important effects on their miscibility with acceptors, affording a chance to tune the morphologies of the corresponding blends.

The GIWAXS measurements were performed to further investigate the structural organizations of the blended films (Figure 4b,c). According to the discussions above, the pure film of three SMDs has co-existed with edge-on and face-on orientations. After blending with the electron acceptor of BTP-eC9, a broad and strong (010) diffraction peak appears in the OOP direction, indicating all blend films show preferred face-on arrangements along with the substrates, which is beneficial for the charge transport from the D:A interfaces towards the electrodes.<sup>[52]</sup> As shown in Figure 4d,e and Table S10 (Supporting Information), the CCL of lamellar stacking in the IP direction for HD-1-based blend film is the largest in three blend films. In addition, the same CCL results can be obtained from  $\pi-\pi$  stacking in the OOP direction. These results explain that

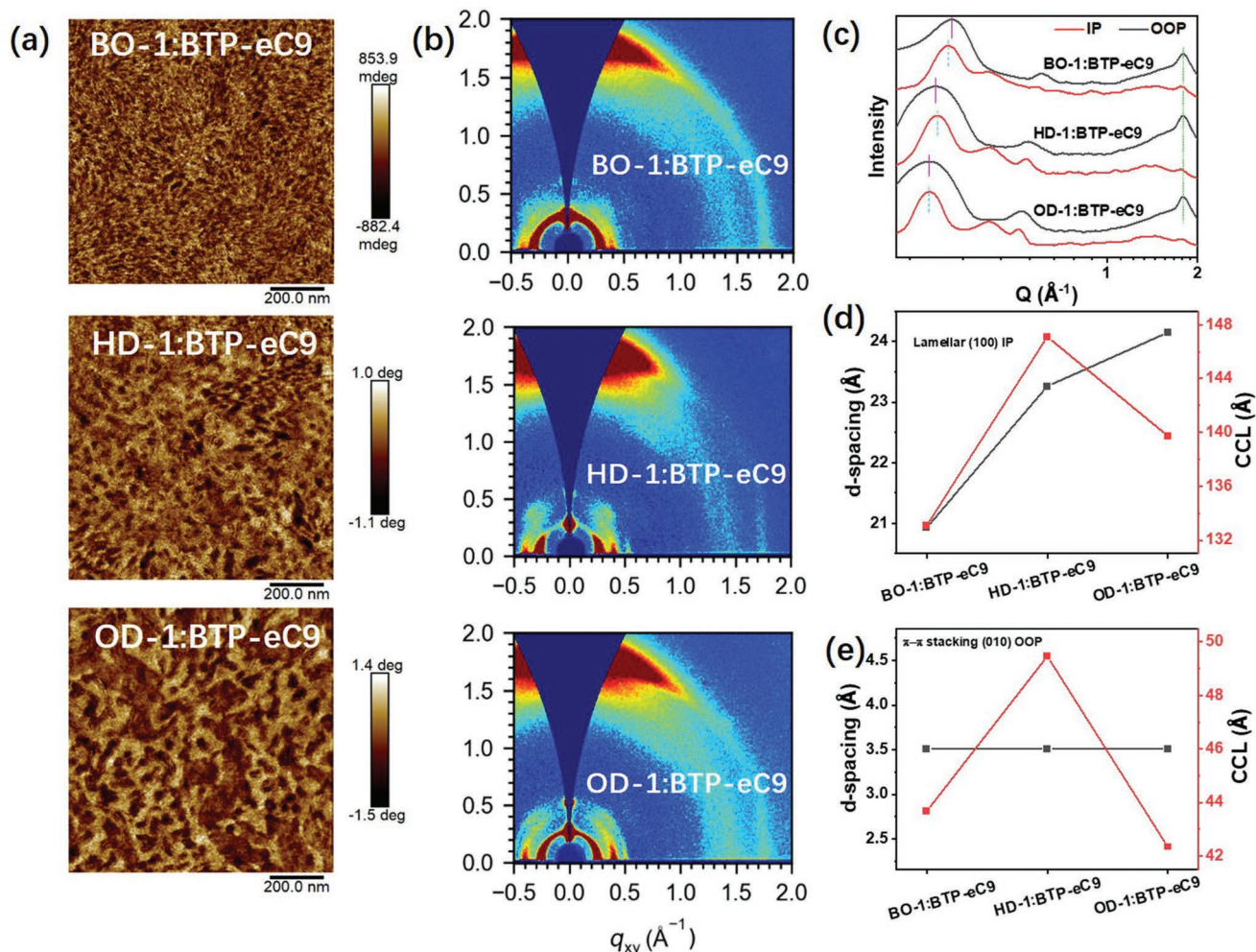


**Figure 4.** a) AFM phase images of the blend films. b) 2D GIWAXS images of the blend films. c) The 1D GIWAXS profiles of the blend films. d) d-spacing and CCL calculated from GIWAXS in lamellar IP direction and e)  $\pi-\pi$  stacking OOP direction.

HD-1:BTP-eC9 blends have slightly higher hole mobility than that of the other two blends. Moreover, the (300) and (400) diffraction peaks in OOP direction that were found in the neat films of the SMDs disappeared in the blend films for all devices (Figure 4c), which suggests that the introduction of the BTP-eC9 suppresses the crystallization of small-molecule donors in the blends.<sup>[27]</sup> In addition, the (300) diffraction peak in the IP direction disappeared in the BO-1-based devices; however, it can be clearly observed in the HD-1 and OD-1-based devices. This indicates that with the increase of chain length, the suppressing effect of BTP-eC9 on higher level (h00) stacking of SMDs weakened.

### 3. Conclusions

To summarize, three A-D-A structured small-molecule donors (BO-1, HD-1, and OD-1) were designed and synthesized by tuning the length of alkyl chain on the thiazole side unit on the BDT unit. These small molecules showed similar optical and electrochemical properties, but their crystallinities gradually became weaker with the elongation of the side

group alkyl chains. Among these three small molecule donors, HD-1-based blended film formed a favorable BHJ morphology with optimized carrier transport and proper phase separation. As a result, the HD-1-based device yielded an outstanding PCE of 17.19% with a  $V_{OC}$  of 0.842 V, a  $J_{SC}$  of 26.04  $\text{mA cm}^{-2}$ , and an FF of 78.28%, which represents one of the highest PCEs among SM-OSCs. These results demonstrated that modulating the molecular alkyl chains on the thiazole side groups of SMDs is important for the optimization of the BHJ morphology and for achieving high-performance SM-OSCs.

### Supporting Information

Supporting Information is available from the Wiley Online Library or from the author.

### Acknowledgements

The authors gratefully acknowledge the financial support from NSFC (21935007, 52025033, 51873089) and MoST (2022YFB4200400,

2019YFA0705900) of China, Tianjin city (20JCZDJC00740), 111 Project (B12015) and the 100 Young Academic Leaders Program of Nankai University (020-ZB22000110 and 023-ZB22000105) and Haihe Laboratory of Sustainable Chemical Transformations. A portion of this work was based on the data obtained at BSRF-1W1A. The authors gratefully acknowledge the cooperation of the beamline scientists at BSRF-1W1A beamline.

## Conflict of Interest

The authors declare no conflict of interest.

## Author Contributions

K.M. and W.F. contributed equally to this work. The synthetic works were carried out by K.M., and W.F. carried out the device fabrication and measurements. Y.C. and B.K. conceived and mentored the research. All authors discussed the results and analyzed the data and commented on the manuscript.

## Data Availability Statement

The data that support the findings of this study are available from the corresponding author upon reasonable request.

## Keywords

alkyl chain tuning, all-small-molecules, Organic solar cells, power conversion efficiency, thiazole substituents

Received: December 22, 2022

Revised: January 23, 2023

Published online:

- [1] C. W. Tang, *Appl. Phys. Lett.* **1986**, *48*, 183.
- [2] G. Yu, J. Gao, J. C. Hummelen, F. Wudl, A. J. Heeger, *Science* **1995**, *270*, 1789.
- [3] J. Zhou, X. Wan, Y. Liu, Y. Zuo, Z. Li, G. He, G. Long, W. Ni, C. Li, X. Su, Y. Chen, *J. Am. Chem. Soc.* **2012**, *134*, 16345.
- [4] Y. Lin, J. Wang, Z. G. Zhang, H. Bai, Y. Li, D. Zhu, X. Zhan, *Adv. Mater.* **2015**, *27*, 1170.
- [5] J. Yuan, Y. Zhang, L. Zhou, G. Zhang, H.-L. Yip, T.-K. Lau, X. Lu, C. Zhu, H. Peng, P. A. Johnson, M. Leclerc, Y. Cao, J. Ulanski, Y. Li, Y. Zou, *Joule* **2019**, *3*, 1140.
- [6] M. Zhang, X. Guo, W. Ma, H. Ade, J. Hou, *Adv. Mater.* **2015**, *27*, 4655.
- [7] X. Wan, C. Li, M. Zhang, Y. Chen, *Chem. Soc. Rev.* **2020**, *49*, 2828.
- [8] M. Li, K. Gao, X. Wan, Q. Zhang, B. Kan, R. Xia, F. Liu, X. Yang, H. Feng, W. Ni, Y. Wang, J. Peng, H. Zhang, Z. Liang, H.-L. Yip, X. Peng, Y. Cao, Y. Chen, *Nat. Photon.* **2017**, *11*, 85.
- [9] Y. Lin, Y. Li, X. Zhan, *Chem. Soc. Rev.* **2012**, *41*, 4245.
- [10] Z. Zheng, J. Wang, P. Bi, J. Ren, Y. Wang, Y. Yang, X. Liu, S. Zhang, J. Hou, *Joule* **2022**, *6*, 171.
- [11] L. Zhu, M. Zhang, J. Xu, C. Li, J. Yan, G. Zhou, W. Zhong, T. Hao, J. Song, X. Xue, Z. Zhou, R. Zeng, H. Zhu, C.-C. Chen, R. C. I. MacKenzie, Y. Zou, J. Nelson, Y. Zhang, Y. Sun, F. Liu, *Nat. Mater.* **2022**, *21*, 656.
- [12] L. Meng, Y. Zhang, X. Wan, C. Li, X. Zhang, Y. Wang, X. Ke, Z. Xiao, L. Ding, R. Xia, H. L. Yip, Y. Cao, Y. Chen, *Science* **2018**, *361*, 1094.
- [13] B. Kan, Q. Zhang, F. Liu, X. Wan, Y. Wang, W. Ni, X. Yang, M. Zhang, H. Zhang, T. P. Russell, Y. Chen, *Chem. Mater.* **2015**, *27*, 8414.
- [14] M. Li, W. Ni, X. Wan, Q. Zhang, B. Kan, Y. Chen, *J. Mater. Chem. A* **2015**, *3*, 4765.
- [15] S. Wu, W. Feng, L. Meng, Z. Zhang, X. Si, Y. Chen, X. Wan, C. Li, Z. Yao, Y. Chen, *Nano Energy* **2022**, *103*, 107801.
- [16] Y. Sun, L. Nian, Y. Kan, Y. Ren, Z. Chen, L. Zhu, M. Zhang, H. Yin, H. Xu, J. Li, X. Hao, F. Liu, K. Gao, Y. Li, *Joule* **2022**, *6*, 2835.
- [17] J. Qin, Z. Chen, P. Bi, Y. Yang, J. Zhang, Z. Huang, Z. Wei, C. An, H. Yao, X. Hao, T. Zhang, Y. Cui, L. Hong, C. Liu, Y. Zu, C. He, J. Hou, *Energy Environ. Sci.* **2021**, *14*, 5903.
- [18] Z. Li, X. Wang, N. Zheng, A. Saparbaev, J. Zhang, C. Xiao, S. Lei, X. Zheng, M. Zhang, Y. Li, B. Xiao, R. Yang, *Energy Environ. Sci.* **2022**, *15*, 4338.
- [19] L. Zhang, R. Sun, Z. Zhang, J. Zhang, Q. Zhu, W. Ma, J. Min, Z. Wei, D. Deng, *Adv. Mater.* **2022**, *34*, 2207020.
- [20] M. Zhang, X. Guo, W. Ma, H. Ade, J. Hou, *Adv. Mater.* **2015**, *27*, 4655.
- [21] H. Yang, C. Cui, Y. Li, *Acc. Mater. Res.* **2021**, *2*, 986.
- [22] C. Cui, Y. Li, *Energy Environ. Sci.* **2019**, *12*, 3225.
- [23] H. Tang, H. Chen, C. Yan, J. Huang, P. W. K. Fong, J. Lv, D. Hu, R. Singh, M. Kumar, Z. Xiao, Z. Kan, S. Lu, G. Li, *Adv. Energy Mater.* **2020**, *10*, 2001076.
- [24] J. Min, Y. N. Luponosov, N. Gasparini, M. Richter, A. V. Bakirov, M. A. Shcherbina, S. N. Chvalun, L. Grodd, S. Grigorian, T. Ameri, S. A. Ponomarenko, C. J. Brabec, *Adv. Energy Mater.* **2015**, *5*, 1500386.
- [25] G. Yang, Z. Li, K. Jiang, J. Zhang, J. Chen, G. Zhang, F. Huang, W. Ma, H. Yan, *Sci. China: Chem.* **2017**, *60*, 545.
- [26] T. Wang, J.-L. Brédas, *J. Am. Chem. Soc.* **2021**, *143*, 1822.
- [27] C. An, Y. Qin, T. Zhang, Q. Lv, J. Qin, S. Zhang, C. He, H. Ade, J. Hou, *J. Mater. Chem. A* **2021**, *9*, 13653.
- [28] B. J. Zhou, L. Wang, Y. Liu, C. H. Guo, D. H. Li, J. L. Cai, Y. W. Fu, C. Chen, D. Liu, Y. H. Zhou, W. Li, T. Wang, *Adv. Funct. Mater.* **2022**, *32*, 2206042.
- [29] R. M. Zhou, Z. Y. Jiang, Y. A. Shi, Q. Wu, C. Yang, J. Q. Zhang, K. Lu, Z. X. Wei, *Adv. Funct. Mater.* **2020**, *30*, 2005426.
- [30] L. Ye, K. Weng, J. Xu, X. Du, S. Chandrabose, K. Chen, J. Zhou, G. Han, S. Tan, Z. Xie, Y. Yi, N. Li, F. Liu, J. M. Hodgkiss, C. J. Brabec, Y. Sun, *Nat. Commun.* **2020**, *11*, 6005.
- [31] Y. Cui, H. Yao, J. Zhang, K. Xian, T. Zhang, L. Hong, Y. Wang, Y. Xu, K. Ma, C. An, C. He, Z. Wei, F. Gao, J. Hou, *Adv. Mater.* **2020**, *32*, 1908205.
- [32] S. Park, D. Seo, K. Kwak, D. S. Chung, C. H. Cheon, B. Kim, H. J. Son, *Dyes Pigm.* **2015**, *123*, 323.
- [33] J.-L. Bredas, *Mater. Horiz.* **2014**, *1*, 17.
- [34] S. Li, L. Zhan, C. Sun, H. Zhu, G. Zhou, W. Yang, M. Shi, C.-Z. Li, J. Hou, Y. Li, H. Chen, *J. Am. Chem. Soc.* **2019**, *141*, 3073.
- [35] C. Sun, S. Qin, R. Wang, S. Chen, F. Pan, B. Qiu, Z. Shang, L. Meng, C. Zhang, M. Xiao, C. Yang, Y. Li, *J. Am. Chem. Soc.* **2020**, *142*, 1465.
- [36] W. L. Tan, C. R. McNeill, *Appl. Phys. Rev.* **2022**, *9*, 021310.
- [37] T. Kumari, S. M. Lee, S.-H. Kang, S. Chen, C. Yang, *Energy Environ. Sci.* **2017**, *10*, 258.
- [38] Y. Zheng, S. Bao, H. Yang, H. Fan, D. Fan, C. Cui, Y. Li, *Chem. Commun.* **2021**, *57*, 10767.
- [39] K. Gao, S. B. Jo, X. Shi, L. Nian, M. Zhang, Y. Kan, F. Lin, B. Kan, B. Xu, Q. Rong, L. Shui, F. Liu, X. Peng, G. Zhou, Y. Cao, A. K. Jen, *Adv. Mater.* **2019**, *31*, 1807842.
- [40] K. Vandewal, J. Benduhn, V. C. Nikolis, *Sustainable Energy Fuels* **2018**, *2*, 538.
- [41] Y. M. Wang, D. P. Qian, Y. Cui, H. T. Zhang, J. H. Hou, K. Vandewal, T. Kirchartz, F. Gao, *Adv. Energy Mater.* **2018**, *8*, 1801352.
- [42] Y. Cui, H. Yao, J. Zhang, K. Xian, T. Zhang, L. Hong, Y. Wang, Y. Xu, K. Ma, C. An, C. He, Z. Wei, F. Gao, J. Hou, *Adv. Mater.* **2020**, *32*, 1908205.

- [43] U. Rau, B. Blank, T. C. M. Müller, T. Kirchartz, *Phys. Rev. Appl.* **2017**, 7, 044016.
- [44] W. Shockley, H. J. Queisser, *J. Appl. Phys.* **1961**, 32, 510.
- [45] K. Vandewal, K. Tvingstedt, A. Gadisa, O. Inganäs, J. V. Manca, *Phys. Rev. B* **2010**, 81, 125204.
- [46] V. C. Nikolis, J. Benduhn, F. Holzmueller, F. Piersimoni, M. Lau, O. Zeika, D. Neher, C. Koerner, D. Spoltore, K. Vandewal, *Adv. Energy Mater.* **2017**, 7, 1700855.
- [47] M. Limpinsel, A. Wagenpfahl, M. Mingeback, C. Deibel, V. Dyakonov, *Phys. Rev. B* **2010**, 81, 085203.
- [48] A. K. K. Kyaw, D. H. Wang, V. Gupta, W. L. Leong, L. Ke, G. C. Bazan, A. J. Heeger, *ACS Nano* **2013**, 7, 4569.
- [49] K. Chong, X. Xu, H. Meng, J. Xue, L. Yu, W. Ma, Q. Peng, *Adv. Mater.* **2022**, 34, 2109516.
- [50] H. Azimi, A. Senes, M. C. Scharber, K. Hingerl, C. J. Brabec, *Adv. Energy Mater.* **2011**, 1, 1162.
- [51] K.-H. Kim, H. Kang, H. J. Kim, P. S. Kim, S. C. Yoon, B. J. Kim, *Chem. Mater.* **2012**, 24, 2373.
- [52] H. Alexander, B. Wim, G. James, S. Eric, G. Eliot, K. Rick, M. Alastair, C. Matthew, R. Bruce, P. Howard, *J. Phys.: Conf. Ser.* **2010**, 247, 012007.